


Isostructural Transition of $\text{Zr}_{0.7}\text{Hf}_{0.15}\text{Nb}_{0.15}\text{Co}_{0.6}\text{Cu}_{0.15}\text{Ni}_{0.25}$ Alloy for Isotope Trapping Minimization and High-Temperature Durability Enhancement

Jiacheng Qi, Xinyi Zhang, Binkai Yu, Xuezhong Xiao*, Fei Chu, Tiao Ying, Xingwen Feng, Jiangfeng Song, Yan Shi, Huaqin Kou*, Changan Chen, Wenhua Luo, and Lixin Chen* 

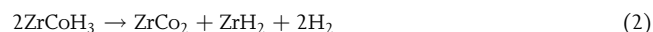
The launch of International Thermonuclear Experimental Reactor project paves the way to wide adoption of DT fusion energy as future energy source. Efficient fuel cycle to minimize strategic tritium inventory proves crucial for commercially viable fusion technologies. ZrCo alloy is considered as a promising candidate for fast isotope handling. However, cycling degradation caused by hydrogen-induced disproportionation results in severe tritium trapping, thus impeding its practical application. Herein, an isostructural transition is successfully constructed with low hysteresis, ameliorated plateau flatness of pressure-composition isotherms and improved high-temperature durability for hydrogen trapping minimization. Specifically, the optimal $\text{Zr}_{0.7}\text{Hf}_{0.15}\text{Nb}_{0.15}\text{Co}_{0.6}\text{Cu}_{0.15}\text{Ni}_{0.25}$ alloy adopts Hf-Nb and Cu-Ni as Zr and Co side doping elements, exhibiting substantial thermodynamic destabilization with nearly 90 °C reduction of delivery temperature, and significant kinetic promotion with a threefold lower energy barrier. More importantly, both hydrogen utilization and cycling retention of optimal alloy are increased by about twenty times compared with pristine alloy after 100 cycles at 500 °C. Minimized disproportionation driving force from both isostructural transition and suppressed 8e hydrogen occupation realizes full potential of optimal alloy. This work demonstrates the effectiveness of combining isostructural transformation and high-temperature durability improvement to enhance the hydrogen utilization of ZrCo-based alloys and other hydrogen storage materials.

1. Introduction

The intensifying severity of energy crisis is prompting an escalating emphasis on the exploration of renewable and efficient carbon-free energy sources.^[1–3] The deuterium-tritium controlled nuclear fusion technology emerges as one of the most promising options due to its substantial energy output and environmental sustainability.^[4] Advancements in hydrogen isotope recovery, storage, and supply technologies are essential for minimization of tritium inventory, thereby safe and efficient operation of fusion reactors which relies on rapid and sufficient provision of deuterium-tritium fuel streams through the fueling system.^[5–7]

ZrCo alloy, characterized with rapid de-/hydrogenation kinetics, low hydrogenation plateau ($\sim 10^{-3}$ Pa at room temperature), effective ^3He trapping and non-radioactivity, is considered a promising alternative material to depleted uranium (DU) in the hydrogen isotope storage and delivery system (SDS) of International Thermonuclear Experimental Reactor (ITER).^[8,9] However, the cycling capacity of de-/hydrogenation typically exhibits a

progressive descent,^[8] and approaches to only 22.4% of initial capacity as cycling proceeds, resulted from the hydrogen-induced disproportionation (HID) reactions, which can be described by following equations^[10,11]



The hydrogen trapped in disproportionation products with highly thermodynamic stability causes continual loss of valid hydrogen storage capacity with cycling.^[12,13] Great efforts have been committed to enhancing anti-disproportionation performance and cycling durability of ZrCo alloy through alloy composition design.^[6,14] Previous findings strongly prove the concept of isostructural transformation critical for anti-disproportionation and cycling stability enhancement. Al/Ti single doping shows a relatively slight improvement in cycling stability with de-/hydrogenation of cubic isostructural phase transition after capacity stabilization.^[15,16] Additionally, doping with Cu and Nb-Cu provides a

J. Qi, X. Zhang, Dr. X. Xiao, F. Chu, T. Ying, Dr. L. Chen
State Key Laboratory of Silicon and Advanced Semiconductor Materials,
School of Materials Science and Engineering, Zhejiang University, Hangzhou
310058, China

E-mail: xiaoxzh6@mail.sysu.edu.cn

E-mail: lxchen@zju.edu.cn

B. Yu


School of Materials and Energy, Yunnan University, Kunming 650091, China
Dr. X. Xiao

School of Advanced Energy, Sun Yat-Sen University, Shenzhen 518107, China
Dr. X. Feng, Dr. J. Song, Dr. Y. Shi, Dr. H. Kou, Dr. C. Chen, Dr. W. Luo
Institute of Materials, China Academy of Engineering Physics, Mianyang
621907, China

E-mail: kouhuaqin@caep.cn

Dr. L. Chen

Key Laboratory of Hydrogen Storage and Transportation Technology of
Zhejiang Province, Hangzhou 310027, China

 The ORCID identification number(s) for the author(s) of this article can be found under <https://doi.org/10.1002/eem2.70000>.

DOI: 10.1002/eem2.70000

platform to achieve an orthorhombic isostructural phase transition between ZrCoH_3 and orthorhombic intermediate hydride phase (B33') with significant cycling stability enhancement by cutoff pressure control.^[17,18] Our group further validated the general effectiveness of constructing orthorhombic isostructural phase transitions to boost the disproportionation resistance and cycling stability of ZrCo alloy through partial substitution by conducive elements for B33 phase formation.^[18–20] With the proposed principle based on the thermodynamic stability gap between cubic B2 and orthorhombic B33 phases, we successfully established a single orthorhombic isostructural phase transition with exceptional cyclic stability by finely modulating the Cu/Ni ratio.^[21]

However, multicomponent doping with orthorhombic favorable elements, e.g. Nb, Cu and Ni, successfully suppresses disproportionation during cycling while impairs plateau property of pressure-composition isotherms (PCIs). A sloping correlation between hydrogen content and equilibrium pressure of PCIs diminishes hydrogen utilization and results in increased hydrogen trapping, especially for batch supply to fuel tanks with certain back pressure in the SDS. It is desirable to maintain orthorhombic isostructural phase transition during de-/hydrogenation while simultaneously ameliorate the plateau property. In addition, elevating the operation temperature is one of the efficient approaches to boost hydrogen utilization and minimize hydrogen trapping. However, the method is limited by the HID reactions positively dependent on temperature and hydrogen pressure.^[10,22]

In this work, due to the merits of high-temperature durability enhancement and plateau amelioration of Hf element,^[23–30] ZrCo-based alloys with Hf/Nb/Hf-Nb doping for Zr side based on previously refined Co-Cu-Ni composition are designed and synthesized. The Hf-Nb co-doping ZrCo-based alloy ($\text{Zr}_{0.7}\text{Hf}_{0.15}\text{Nb}_{0.15}\text{Co}_{0.6}\text{Cu}_{0.15}\text{Ni}_{0.25}$ alloy) exhibits significant thermodynamical destabilization, kinetic promotion, plateau flatness improvement and high-temperature durability enhancement. More importantly, the optimal alloy exhibits outstanding hydrogen utilization of 95.40% and cycling retention of 95.95%, which are increased by about twenty times compared with the pristine alloy after 100 cycles at 500 °C. This work substantiates the potential of combining isostructural transition with synergistic doping of anti-disproportionation favorable elements in facilitating fuel cycle and minimizing tritium inventory for next-generation fusion reactors.

2. Results and Discussion

2.1. Design of Low Hydrogen Trapping Alloys

Due to the positive effect of Hf doping to hoist high-temperature durability and plateau flatness,^[21,23–30] ZrCo-based alloys with Hf/Nb/Hf-Nb doping for Zr side based on previously refined Co-Cu-Ni composition are designed and synthesized. As compared to undoped ZrCo alloy with single CsCl-type cubic structure (space group: $\text{Pm}\bar{3}\text{m}$, labeled as B2), the formation of CrB-type orthorhombic structure (space group: Cmcm , labeled as B33) is detected in $\text{Zr}_{0.85}\text{Nb}_{0.15}\text{Co}_{0.6}\text{Cu}_{0.15}\text{Ni}_{0.25}$ (NCN), $\text{Zr}_{0.7}\text{Nb}_{0.3}\text{Co}_{0.6}\text{Cu}_{0.15}\text{Ni}_{0.25}$ (N2CN), $\text{Zr}_{0.85}\text{Hf}_{0.15}\text{Co}_{0.6}\text{Cu}_{0.15}\text{Ni}_{0.25}$ (HCN), $\text{Zr}_{0.7}\text{Hf}_{0.3}\text{Co}_{0.6}\text{Cu}_{0.15}\text{Ni}_{0.25}$ (H2CN), and $\text{Zr}_{0.7}\text{Hf}_{0.15}\text{Nb}_{0.15}\text{Co}_{0.6}\text{Cu}_{0.15}\text{Ni}_{0.25}$ (HNCN) alloys by X-ray diffraction (XRD) (Figure 1a). Indicated by the wide proportion range of B33 and B2 phase, doping with

orthorhombic-favorable elements, that is, Nb, Cu, and Ni, against cubic-favorable element such as Hf provides us a strategy to tailor phase components. The XRD patterns illustrate that Hf doping in HNCN alloy preserves the main phase of B33, which favors targeting isostructural orthorhombic phase transition during de-/hydrogenation. However, excessive Hf/Nb single doping for Zr side in H2CN and N2CN alloys almost suppress the formation of B33 phase and introduce noticeable second phases, respectively. Therefore, NCN, HCN, and HNCN alloys with B33 main phase will be discussed in detail. Scanning electron microscopy (SEM) and transmission electron microscopy (TEM) combined with energy dispersive X-ray spectroscopy (EDS) were utilized to examine the chemical homogeneity of NCN, HCN and HNCN alloys (Figure 1b and Figure S1, Supporting Information). The absence of elemental segregation in the EDS and impurity phases in the XRD patterns suggests valid solid solution of multiple doping elements. Moreover, the detailed lattice parameters and phase component of ZrCo, NCN, HCN, and HNCN alloys were calculated by Rietveld refinement based on the XRD patterns (Figure 1c and Figures S2–S4, Supporting Information), and are given in Table 1. The decrease trend of orthorhombic lattice volume from HCN to NCN and further to HNCN can be revealed, in line with the high-angle shift of major diffraction peaks, due to atomic size effect. In addition, TEM image, corresponding selected-area electron diffraction (SAED) pattern and high-resolution TEM (HRTEM) image identify the co-existence of B33 and B2 phases in HNCN alloy, aligning with the XRD results (Figure 1d,e).

Thermodynamic behaviors at constant temperature illustrate that Hf-Nb co-doping exhibits more substantial thermodynamic destabilization effect compared with Nb/Hf single doping for Zr side (Figure 1f), which is consistent with Lundin theory^[31] and originating from the notable disparity in the atomic size and hydrogen affinity. Except for ZrCo alloy, all PCI curves of HCN, NCN, and HNCN alloys exhibit negligible pressure hysteresis between de-/hydrogenation curves, which arises from lattice strain induced by lattice expansion and shrinkage during hydrogen absorption and desorption.^[32,33] This indicates a significantly alleviated lattice strain and volume variation for orthorhombic isostructural phase transition of multicomponent alloys compared to cubic-to-orthorhombic transition of ZrCo alloy. Enhancement of delivery performance commonly prohibits hydrogen isotope storage process, while such non-hysteresis characteristic give a solution to this paradox. It is desirable to facilitate desorption process meanwhile maintain fast absorption kinetic and storage capacity, which validated by absorption kinetic measurements at room temperature and saturated hydride phase (Figures S5 and S6, Supporting Information). To evaluate hydrogen trapping, the plateau slope factor (S_p) was calculated from PCIs as an indication of hydrogen utilization and residual hydrogen content (Table 2). Overall, further Hf doping based on NCN alloy helps to facilitate hydrogen release with plateau elevation and reduce hydrogen retention with flat plateau character.

Thermodynamic parameters for dehydrogenation were deduced by Van't Hoff equation (Eq. 3) which correlates the equilibrium pressure (P_{eq}) as a function of reciprocal kelvin temperature and thermodynamic properties (Figure 1g and Figure S7, Supporting Information). (Detailed value are listed in Table 2). The dehydrogenation enthalpy decreases from 86.00 to 75.41 $\text{kJ}\cdot\text{mol}^{-1}$ H_2 , manifesting reduced thermodynamic stability of hydride and more accessible supply operation, confirmed by decreased operation temperature for atmospheric pressure delivery (T_1 bar).

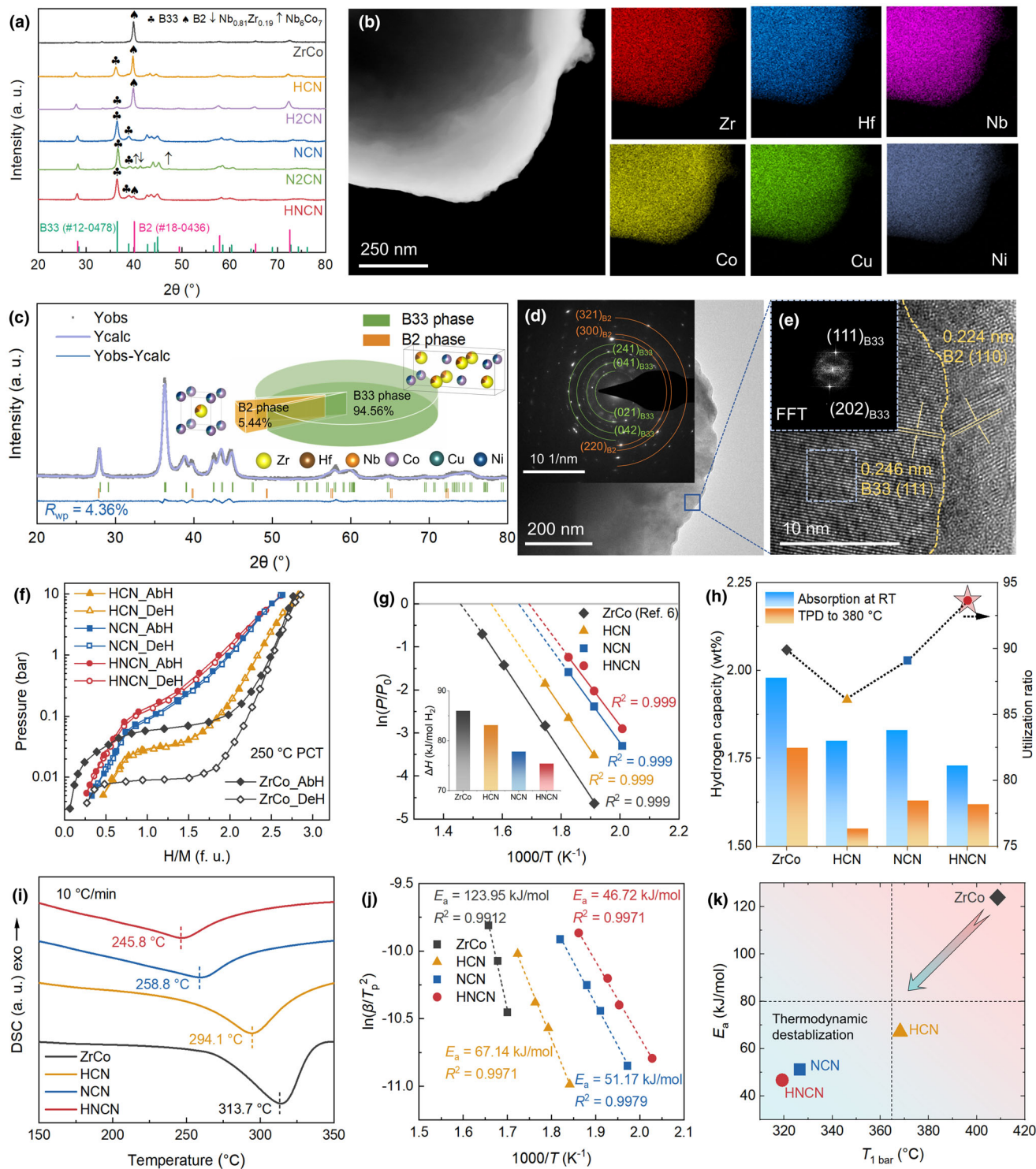


Figure 1. a) XRD patterns of as-cast ZrCo, HCN, H2CN, NCN, N2CN, and HNCN alloys. b) HAADF-STEM image and corresponding EDS elemental mapping. c) Rietveld refinement results, d) TEM image and corresponding SAED pattern, e) HRTEM image and the inset shows the fast Fourier transform (FFT) of the region of interest with blue dash line of HNCN alloy. f) De-/hydrogenation PCT curves at 250 °C where AbH and DeH represent hydrogen absorption and desorption processes, respectively, g) Van't Hoff plots and the inset shows the enthalpy change of dehydrogenation reaction, h) Capacity of hydrogen storage at room temperature (RT) and TPD from room temperature to 380 °C, and corresponding hydrogen utilization ratio, i) DSC curves at the heating rate of 10 °C min⁻¹, j) Kissinger fitting profiles, and k) Kinetic activation energies (E_a) for dehydrogenation and thermodynamic operation temperature for atmospheric pressure delivery ($T_{1 \text{ bar}}$) of ZrCo, HCN, NCN, and HNCN alloys.

Table 1. Lattice parameters and phase components as well as saturated hydrogen storage capacities of ZrCo, HCN, NCN, and HNCN alloys.

Compositions	Lattice parameters of B33 phase				Phase component (%)		C_{\max}^a (wt%)
	a/Å	b/Å	c/Å	V/Å ³	B33	B2	
ZrCo	3.5356	10.5017	4.3175	160.31	0	100	1.930
HCN	3.2426	9.8411	4.1622	132.82	62.76	37.24	1.787
NCN	3.2296	9.8925	4.1445	132.41	98.01	1.99	1.841
HNCN	3.2228	9.8701	4.1437	131.81	94.56	5.44	1.815

^a C_{\max} is the saturated hydrogen storage capacity at room temperature.

$$\ln P_{\text{eq}} = -\frac{\Delta H}{RT} + \frac{\Delta S}{R} \quad (3)$$

Taken as an analogue SDS operation, temperature programmed desorption (TPD) from room temperature to 380 °C toward a pre-vacuumed vessel (Figure S8, Supporting Information) demonstrate a consistent trend of delivery performance with DSC and PCI measurements. In light of the competitive relationship in kinetics between dehydrogenation and disproportionation reactions,^[13] the facile release of interstitial hydrogen of HNCN hydride contributes to anti-disproportionation enhancement. Furthermore, limit tritium trapping in the tritium-related facility is essential for minimizing the initial tritium inventory and therefore enabling DT fusion power as a practical energy source. The extent of hydrogen utilization is defined as the ratio of TPD and saturated absorption capacity to evaluate the hydrogen trapping during fuel supply operation. There is a sharp increase of hydrogen utilization ratio for HNCN (93.10%) compared with ZrCo (89.90%), HCN (86.11%), and NCN (89.07%) alloys due to thermodynamic destabilization and amelioration of plateau property (Figure 1h).

Additionally, reduced peak temperature and broadened desorption temperature range can be observed for HNCN alloy compared with ZrCo, HCN, and NCN using differential scanning calorimetry (DSC) (Figure 1i). Abundant chemical complexity of interstitial environment induced by multicomponent substitution renders HNCN hydride sequential release of interstitial hydrogen atoms and thereby fairly fast kinetics at readily attainable temperature.^[18,20] Adopting Kissinger equation with series of peak temperatures (T_p) under different heating rates (β), the apparent activation energy barrier (E_a) of

dehydrogenation reaction can be determined (Figure 1j and Figure S9, Supporting Information), which can be described as follows:^[34]

$$\ln \frac{\beta}{T_p^2} = -\frac{E_a}{RT_p} + \ln \frac{AR}{E_a} \quad (4)$$

where A and R signify the pre-exponential factor and molar gas constant, respectively. Therefore, HNCN alloy manifests best hydrogen delivery performance from both thermodynamic and kinetic aspects. Specifically, the E_a of HNCN hydride exhibits three times less than ZrCo hydride. And the $T_{1 \text{ bar}}$ extrapolated by thermodynamic parameters reduced by 90 °C compared with pristine hydride (Figure 1k).

2.2. Cycling Performance and Phase Transition

Improved equilibrium pressure and flatness of plateau region benefit residual hydrogen reduction for HNCN alloy. Moreover, cycling stability enhancement is of paramount importance for eliminating the hydrogen trapping in disproportionation products. Figure 2a illustrates the cycling capacity profiles of ZrCo, HCN, NCN, and HNCN alloys. The cycling capacities and capacity retention rates after 100 cycles are 0.40 wt% (22.47%), 1.44 wt% (92.90%), 1.63 wt% (100%), and 1.62 wt% (100%), respectively. Both HNCN and NCN alloys achieve 100% capacity retention after 100 cycles while the highest hydrogen utilization ratio is achieved for HNCN alloy (93.10%) (Figure 2b and Table S1, Supporting Information). There is no disproportionation phase can be detected after cycling (Figure 2c). Additionally, the B2 phase content after one cycle is notably reduced compared to the as-cast counterpart. To track the phase transition path of HNCN hydride during dehydrogenation, XRD analysis was performed on the intermediate dehydrogenated phases under different desorption cutoff pressures (Figure 2e), as marked on the dehydrogenation PCI curve at 380 °C (Figure 2d). Specifically, P2 signifies the cycling desorption cutoff pressure. In the case of the cutoff pressure below P2, even approaching vacuum, samples retain the orthorhombic B33 phase, thus highlighting great structural stability. Slight high-angle shifts of diffraction peaks with decreased hydrogen content indicate the release of solid-solution hydrogen. It can be inferred that HNCN alloy undergoes a single isostructural phase transition (B33 ↔ ZrCoH₃) during 380 °C cycling.

In accordance with previously reported literature,^[16] the de-/hydrogenation pathway of ZrCo alloy (Figure 2f) evolves from cubic B2 phase ↔ orthorhombic ZrCoH₃ phase to cubic B2 phase ↔ cubic B2' phase, corresponding to solid-solution hydrogen absorption and

Table 2. Thermodynamic parameters for dehydrogenation of HNCN, NCN, and HCN alloys.

Compositions	P_{eq}^a (bar)				S_f^b	ΔH (kJ·mol ⁻¹ H ₂)	ΔS (J·K ⁻¹ ·mol ⁻¹ H ₂)	$T_{1 \text{ bar}}^c$ (°C)
	225 °C	250 °C	275 °C	300 °C				
HNCN	0.060	0.133	0.290	–	0.77	75.41	127.30	319.2
NCN	0.033	0.088	0.208	–	0.91	77.80	128.80	326.5
HCN	–	0.030	0.071	0.157	0.34	83.11	129.59	368.2

^a P_{eq} is the equilibrium plateau pressure for hydrogen desorption.

^b S_f is the plateau slope factor of dehydrogenation PCI curve at 250 °C. $S_f = \ln(P_1/P_2)$, where P_1 and P_2 denote the pressures of right and left inflection points, respectively.

^c $T_{1 \text{ bar}}$ is the required desorption temperature for delivery of 1 bar hydrogen.

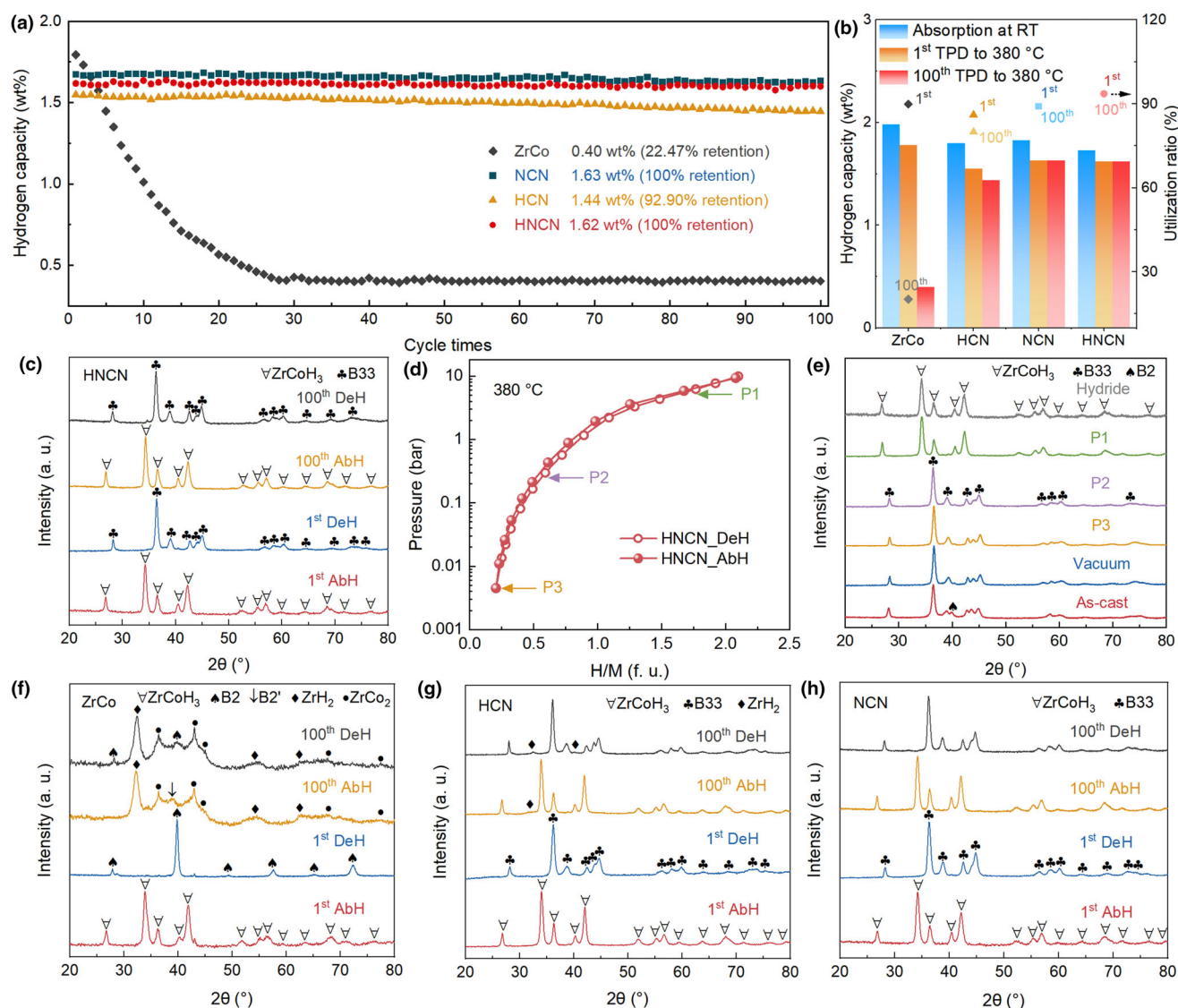


Figure 2. a) Cyclic capacity curves of ZrCo, HCN, NCN, and HNCN samples at 380 °C. b) Hydrogen storage capacity and hydrogen utilization ratio after the 1st and 100th cycles. c) XRD patterns of the de-/hydrogenated samples of HNCN alloy after the 1st and 100th cycles. d) De-/hydrogenation PCI curves at 380 °C of HNCN alloy, and e) XRD patterns corresponding to different desorption cutoff pressures at 380 °C. XRD patterns of the de-/hydrogenated samples of f) ZrCo, g) HCN, and h) NCN alloys after the 1st and 100th cycles. Vacuum represents dehydrogenated state through vacuuming at 380 °C for 15 min.

desorption in the cubic structure, culminating in capacity stabilization. Hence, the phase transition process of HNCN alloy significantly differs from that of ZrCo alloy, maintaining the orthorhombic isostructural characteristic throughout cycling. Isostructural phase transition without long-range atomic migration and rearrangement effectively strengthens the disproportionation resistance of HNCN alloy.^[16,18,35] Similarly, both HCN and NCN alloys exhibit a single orthorhombic isostructural transition during cycling, thereby showcasing remarkably enhanced cycling stability over ZrCo alloy (Figure 2g,h). Additionally, Figures S10 and S11, Supporting Information display the cycling capacity and corresponding XRD profiles of N2CN and H2CN alloys. The cycling capacities and capacity retention rates of N2CN and H2CN alloys after 100 cycles are 1.47 wt% (99.32%) and 1.24 wt% (83.78%)

due to the weak hydrogenation activity of second phases and cubic-to-orthorhombic phase transition, respectively.

2.3. High-Temperature Disproportionation Behavior and its Mechanism

Cycling measurements at 380 °C reveal that HCN, NCN and HNCN alloys all exhibit excellent cycling performance. For realizing the full potential of storage capacity, an elevated temperature of 500 °C was employed to further assess high-temperature disproportionation resistance. Static isothermal disproportionation measurements were conducted at 1 bar and 500 °C for 12 h. Under such an extreme condition,

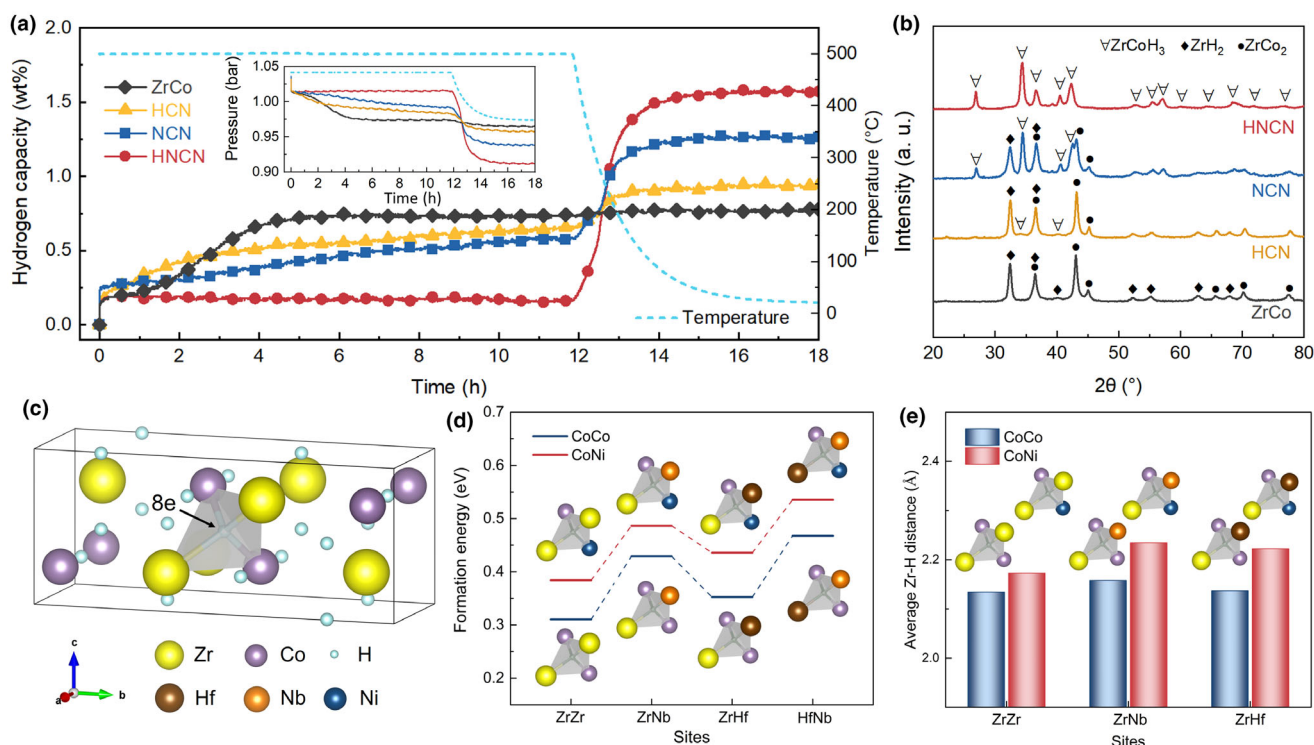


Figure 3. a) Static isothermal disproportionation curves expressed by hydrogen capacity and pressure at 500 °C followed by further cooling process to room temperature and b) XRD patterns after disproportionation at 500 °C for ZrCo, HCN, NCN and HNCN alloys. c) Schematic diagram of the 8e tetrahedral interstitial site. d) Formation energy and e) average Zr-H distance of 8e sites with different atomic configurations.

alloys undergo minor solid-solution hydrogen absorption within alpha phase region because the pressure is far below the equilibrium plateau pressure for hydrogenation and far above that for hydrogenation disproportionation. Subsequently, hydrogenation disproportionation takes place during insulation period as a result of both thermodynamic and kinetic conditions. **Figure 3a** depicts hydrogen capacity and pressure over time, while **Figure 3b** presents the XRD patterns after measurements. According to the disproportionation profiles, ZrCo alloy is almost completely converted to stable disproportionation phases after approximately 5 h. Both Hf and Nb substitutions are found to remarkably improve the anti-disproportionation performance, consistent with previous research,^[23,24,28,36] and further enhancement can be achieved in H2CN and N2CN alloys with increased substituent amounts (Figures S12 and S13, Supporting Information). Comparatively, Nb single doping allows for better anti-disproportionation than Hf single doping for Zr side. Furthermore, Hf-Nb co-doping exhibits a synergistic effect,^[37] endowing HNCN alloy with superior high-temperature durability, with minimal decay extent during isothermal disproportionation at 500 °C.

The principal driving force for disproportionation originates from the occupation of hydrogen atoms in the less stable 8e interstitial sites with short Zr-H distances, which predisposes these atoms to participate in the formation of ZrH₂.^[38,39] Elemental doping can effectively enhance disproportionation resistance by directly reducing the size of 8e site, preventing hydrogen occupancy in 8e sites, and increasing the Zr-H (8e) distances.^[25–27,40,41] First-principles calculations were applied to reveal the intrinsic mechanism of Hf-Nb co-doping on the advancement of disproportionation resistance. The 8e site, illustrated in

Figure 3c, is a tetrahedral interstice composed of 2 Zr and 2 Co atoms. The most prevalent configurations of Co-Co and Co-Ni were considered as Co side atomic configuration. On the other hand, Hf and Nb doping were introduced on the Zr side to obtain 8e sites with diverse atomic configurations, including Zr-Zr, Zr-Nb, Zr-Hf, and Hf-Nb. The resulting formation energies (**Figure 3d**), Zr-H distances (**Figure 3e**), charge transfer (Figures S14 and S15, Supporting Information) of the interstitial 8e sites with different atomic configurations were presented.

In terms of structure, energy and charge transfer, 8e sites with Co-Ni configuration are less susceptible to hydrogen occupation compared to the counterpart with Co-Co configuration. And the propensity of hydrogen atoms in 8e sites to bond with surrounding Zr atoms to form ZrH₂ is apparently weakened due to the increase in Zr-H distance and decrease in electronic interaction. This observation accords with published conclusions that the alleviation effect of Ni doping on disproportionation.^[21,41,42] Besides, the configuration with Zr-Nb is found to be more effective in enhancing disproportionation resistance than the one with Zr-Hf with identical Co side configuration. As expected, the Hf-Nb configuration has the most positive formation energy of hydrogen occupation in 8e sites, which agrees well with the minimum disproportionation extent of HNCN alloy.

2.4. High-Temperature Cycling Performance and Phase Transition

Cycling Based on the aforementioned discussion, HNCN exhibit most appreciable thermodynamic destabilization, significant kinetic

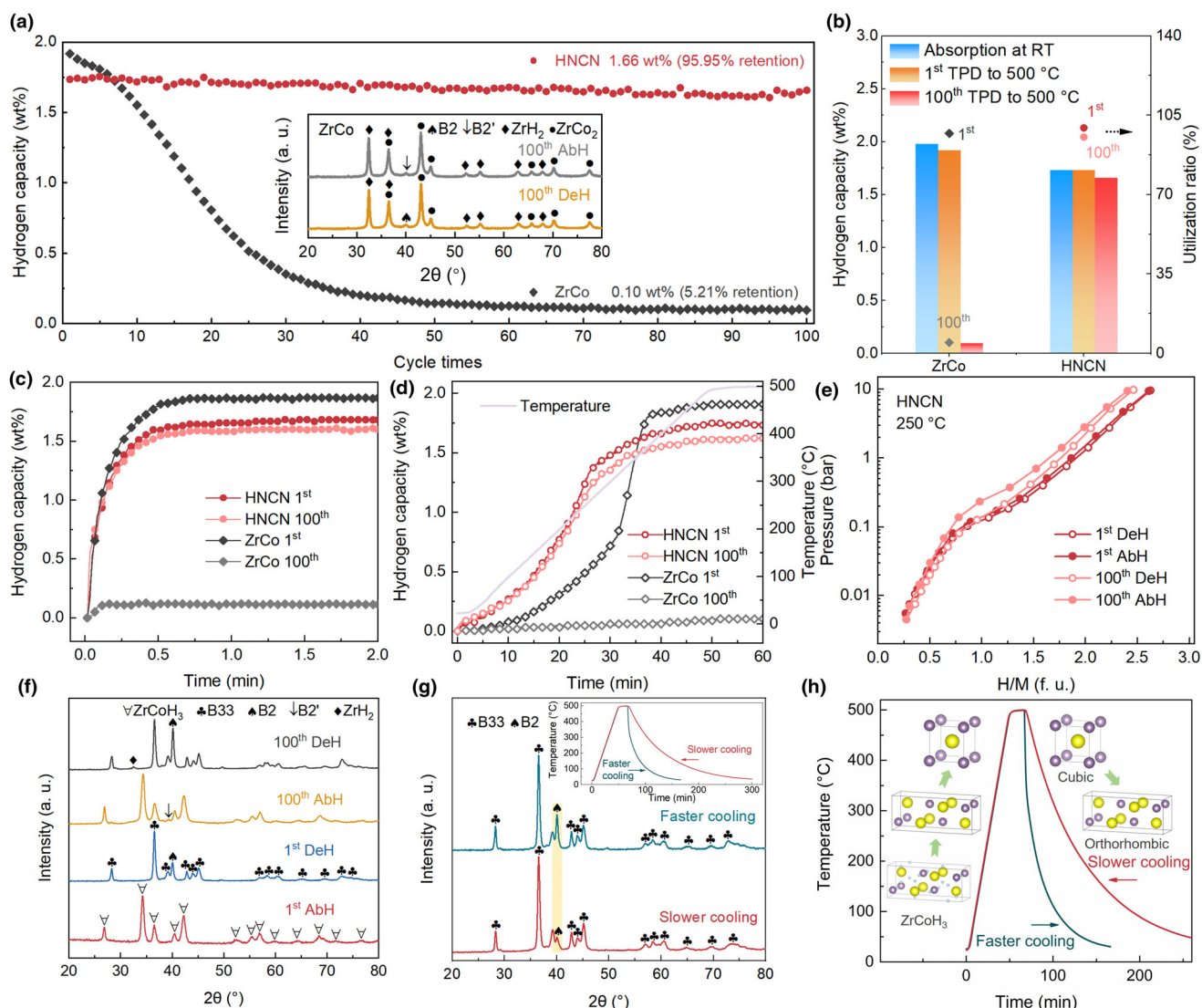


Figure 4. a) Cyclic capacity curves of ZrCo and HNCN alloys at 500 °C. b) Hydrogen storage capacity and hydrogen utilization ratio after 1st and 100th cycles of ZrCo and HNCN alloys. c) Hydrogenation kinetics curves at room temperature and d) dehydrogenation kinetics curves of ZrCo and HNCN samples at the 1st and 100th cycles. e) De-/hydrogenation PCI curves at 250 °C of HNCN alloy at the 1st and 100th cycles. f) XRD patterns of the de-/hydrogenated samples of HNCN alloy after the 1st and 100th cycles. g) XRD patterns of HNCN alloy with different cooling rates after the dehydrogenation up to 500 °C and h) Temperature profiles as well as schematic diagrams of phase transitions during the heating and cooling processes.

facilitation, noticeably improved plateau flatness, increased hydrogen utilization and supereminent cycling stability with outstanding high-temperature durability. Accordingly, the cycling stability of HNCN alloy under extreme condition (cycling delivery temperature up to 500 °C) was further investigated and the cyclic capacity curves of ZrCo and HNCN alloys are shown in **Figure 4a**. It is observed that ZrCo alloy almost completely lose valid storage capacity after 100 cycles (0.10 wt % with 5.21% capacity retention). The inset XRD patterns evidence that only a tiny residual B2 phase undergoes stable solid-solution de-/hydrogenation. In contrast, HNCN alloy demonstrates excellent cycling stability, retaining 1.66 wt% capacity and achieving 95.95% capacity retention after 100 cycles. The hydrogen utilization ratio of HNCN alloy reach 95.40% compared with 5.05% of pristine ZrCo alloy (Figure 4b and Table S2, Supporting Information). Additionally, Figure 4c,d illustrate the pronounced superiority of the hydrogen

absorption/desorption kinetics of HNCN sample over ZrCo after 100 cycles, further highlighting its exceptional high-temperature cycling stability. From a thermodynamic perspective, the de-/hydrogenation PCI curves at 250 °C before and after cycling indicate that HNCN alloy experiences a minor capacity loss accompanied by a slight increase in pressure hysteresis (Figure 4e). These observations demonstrate the impressive stability of HNCN alloy and a slight increase in lattice volume variation after cycling.

XRD analysis of HNCN samples before and after 100 cycles (Figure 4f) reveals a noticeable increase in the B2 phase content in the dehydrogenated state after first dehydrogenation. Reverse martensitic transformation (RMT, B33 → B2) is assumed to be the major reason of B2 content increase.^[20] To validate this hypothesis, two distinct cooling rates were applied to the samples after dehydrogenation (the faster one is 6 °C min⁻¹ and the slower one 2 °C min⁻¹ in average). The XRD

analysis of the samples with different cooling rates indicates that the faster cooling is, the higher B2 phase content is (Figure 4g). Schematic representation of the whole phase transformation process during heating and cooling is provided (Figure 3g). The B33 phase, generated during dehydrogenation of the saturated hydride at moderate temperatures, undergoes RMT into B2 phase with temperature elevated. Subsequently, incomplete martensitic transformation (MT) occurs with increased proportion of B2 phase when cooling fast. An increment in surface relief morphology, one of the major characteristics of MT, is further confirmed by SEM imaging of HNCN samples before and after 100 cycles (Figures S16 and S17, Supporting Information).

The structural stability of B2 phase escalates with accumulated cycling stress and defects based on intrinsic local chemical disordering by multicomponent design.^[43,44] Consequently, a substantial increase in B2 phase is detected in the dehydrogenated sample after 100 cycles (Figure 4f). The B2 phase originating from incomplete MT is not prone to transforming into ZrCoH₃ during hydrogen adsorption, but instead undergoes solid-solution hydrogen absorption to form B2' phase after cycling. The solid-solution hydrogen storage capacity of B2' phase is much lower in comparison to the saturated hydride, leading to a minor capacity loss. The 4.05% capacity degradation rate after 100 cycles can, thus, be ascribed to the raised B2' phase content and slight disproportionation.

3. Conclusion

In this work, a series of ZrCo-based alloys with Hf/Nb/Hf-Nb doping for Zr side under the premise of previously refined Co-Cu-Ni composition are designed and fabricated. Isostructural de-/hydrogenation reactions are successfully established in Zr_{0.7}Hf_{0.15}Nb_{0.15}Co_{0.6}Cu_{0.15}Ni_{0.25} alloy, simultaneously featuring significant thermodynamic destabilization and kinetic promotion. Moreover, negligible PCI hysteresis and improved plateau flatness enable enhanced hydrogen utilization of 93.10% and further 99.43% at 380 and elevated temperature of 500 °C for HNCN alloy. The optimal alloy demonstrates exceptional cycling stability of 1.62 wt% (100% retention) and 1.66 wt% (95.95% retention) after 100 cycles at 380 and 500 °C, respectively. Both the formation of B2' phase from incomplete MT and high-temperature disproportionation are responsible for the minor capacity decay at 500 °C. Static isothermal disproportionation tests at 500 °C also demonstrate its supereminent high-temperature structural stability and disproportionation resistance. First-principles calculations highlight the synergistic effect of Hf-Nb co-substitution on anti-disproportionation with prevention of interstitial 8e hydrogen occupation and formation of ZrH₂. Our cooperative strategy of coupling synergistic elemental substitution with isostructural phase transition effectively optimizes the performance of ZrCo-based alloys as promising hydrogen isotope storage materials, promoting their potential applications in hydrogen isotope handling fields.

4. Experimental Section

Sample preparation: Utilizing high-purity metal raw materials, Zr_{1-x-y}Hf_xNb_yCo_{0.6}Cu_{0.15}Ni_{0.25} ($x, y = 0, 0.15, 0.3$) ingots were prepared via induction levitation melting in a water-cooled copper crucible under a high-purity argon atmosphere. Each ingot was turned over and underwent four remelting cycles to ensure chemical homogeneity. For initial activation, the obtained ingots were cleaned, polished to remove the surface oxide layer, sectioned into pieces, and

then placed in a reactor under vacuum at 500 °C for 1 h. After cooling the reactor to 100 °C, approximately 10 bar of hydrogen was introduced and maintained for several hours until the ingots were completely activated and pulverized into hydride powder.^[45] The as-prepared hydrogenated samples were stored in a glove box filled with high-purity argon for subsequent experiments. Zr_{0.85}Nb_{0.15}Co_{0.6}Cu_{0.15}Ni_{0.25}, Zr_{0.7}Nb_{0.3}Co_{0.6}Cu_{0.15}Ni_{0.25}, Zr_{0.85}Hf_{0.15}Co_{0.6}Cu_{0.15}Ni_{0.25}, Zr_{0.7}Hf_{0.3}Co_{0.6}Cu_{0.15}Ni_{0.25} and Zr_{0.7}Hf_{0.15}Nb_{0.15}Co_{0.6}Cu_{0.15}Ni_{0.25} alloys are denoted as NCN, N2CN, HCN, H2CN, and HNCN, respectively.

Microstructure characterization: Phase constituents were characterized via X-ray diffraction (XRD) analysis on an X'Pert Pro X-ray diffractometer (PANalytical) with Cu K α radiation at 40 kV and 40 mA. Lattice parameters and phase abundances were determined through Rietveld refinement using the *FullProf Suite* software. Microstructure and elemental distribution were observed by scanning electron microscopy (SEM, Hitachi SU-70) and transmission electron microscopy (TEM, Tecnai G2 F20 S-TWIN), both equipped with energy dispersive spectroscopy (EDS).

Hydrogen storage properties measurements: A series of hydrogen storage performance tests were conducted using a Sievert's type apparatus. Hydrogen absorption kinetics were measured under high-purity hydrogen atmosphere of approximately 1.2 bar at room temperature (RT). Hydrogen desorption kinetics were assessed through temperature-programmed desorption (TPD) from room temperature to 380 °C at a heating rate of 10 °C min⁻¹. Thermodynamic characteristics were obtained via pressure-composition isotherm (PCI) measurements through a step-by-step method to complete the entire de-/hydrogenation reaction at fixed temperatures. Differential scanning calorimetry (DSC) was measured on a Netzsch STA449F3 analyzer from room temperature to 600 °C at different heating rates of 5, 8, 10, and 15 °C min⁻¹ under flowing argon.

Cycling tests involve room-temperature hydrogenation under 1.2 bar of high-purity hydrogen and dehydrogenation into a pre-evacuated gas vessel (about 900 mL) from room temperature to 380 and 500 °C with a heating rate of 10 °C min⁻¹, followed by a 10-min insulation, respectively.

To investigate the high-temperature hydrogenation disproportionation behavior, static isothermal disproportionation measurements were conducted. The activated sample was dehydrogenated at 500 °C for 1 h under dynamic vacuuming, then about 1 bar of hydrogen was introduced into the reactor through the gas vessel with the temperature maintained at 500 °C. The reactor was held for 12 h and then cooled to room temperature. Under such condition, the hydrogenation disproportionation can be separated from hydrogenation, and thereby the kinetics and extent of hydrogenation disproportionation can be evaluated based on the decrease in system pressure. The sample loading in the reactor is approximately 0.5 g for all above measurements.

First-principles calculations: First-principles calculations in this work were conducted using the Vienna Ab Initio Simulation Package (VASP), based on density functional theory (DFT) and the projected augmented wave (PAW) method.^[46] Electronic exchange-correlation effects were described using the generalized gradient approximation (GGA) of Perdew-Burke-Ernzerhof (PBE).^[47] The crystal structure construction and computational result visualization including set charge difference were performed using the Visualization for Electronic and Structural Analysis (VESTA) software.^[48] To optimize the structure of 8e sites with various atomic configurations, a 2 × 1 × 2 supercell of orthorhombic ZrCoH₃ was constructed as the initial computational model. Specifically, a plane wave cutoff energy of 400 eV was conducted, with convergence criteria for total energy difference between cycles and residual forces of 10⁻⁶ eV and 0.01 eV Å⁻¹, respectively. A k-point mesh of 3 × 2 × 3 was utilized for the Brillouin zone sampling. The energies of the system with (E_1) and without (E_2) hydrogen occupation in the 8e site were calculated, and the formation energy (E_f) for the H(8e) is defined as below:

$$E_f = E_1 - E_2 - \frac{1}{2}E_{H_2} \quad (5)$$

Acknowledgements

J.Q. and X.Z. contributed equally to this work. We are grateful for the financial supports from the National Key Research and Development Program of China (2022YFE03170002) and the National Natural Science Foundation of China (52071286 and U2030208).

Conflicts of Interest

The authors declare no conflict of interest.

Supporting Information

Supporting Information is available from the Wiley Online Library or from the author.

Keywords

high-temperature durability, hydrogen trapping, isostructural phase transition, ZrCo-based alloys

Received: December 30, 2024

Revised: January 15, 2025

Published online: January 20, 2025

- [1] H. Lund, *Energy* **2007**, 32, 912.
- [2] L. Schlapbach, A. Züttel, *Nature* **2001**, 414, 353.
- [3] G. Liu, D. Chen, Y. Wang, K. Yang, *J. Mater. Sci. Technol.* **2018**, 34, 1699.
- [4] J. Nowotny, T. Hoshino, J. Dodson, A. J. Atanacio, M. Ionescu, V. Peterson, K. E. Prince, M. Yamawaki, T. Bak, W. Sigmund, T. N. Veziroglu, M. A. Alim, *Int. J. Hydrog. Energy* **2016**, 41, 12812.
- [5] M. Rethinasabapathy, S. M. Ghoreishian, S. K. Hwang, Y. K. Han, C. Roh, Y. S. Huh, *Adv. Mater.* **2023**, 35, 2301589.
- [6] Z. Liang, X. Xiao, J. Qi, H. Kou, L. Chen, *J. Alloys Compd.* **2023**, 932, 167552.
- [7] J. Qi, X. Huang, X. Xiao, X. Zhang, P. Zhou, S. Zhang, R. Li, H. Kou, F. Jiang, Y. Yao, J. Song, X. Feng, Y. Shi, W. Luo, L. Chen, *Nat. Commun.* **2024**, 15, 2883.
- [8] W. T. Shmayda, A. G. Heics, N. P. Kherani, *J. Less Common Met.* **1990**, 162, 117.
- [9] F. Wang, R. Li, C. Ding, W. Tang, Y. Wang, S. Xu, R. Yu, Y. Wu, *Prog. Nat. Sci. Mater. Int.* **2017**, 27, 58.
- [10] M. Devillers, M. Sirc, R. D. Penzhorn, *Chem. Mater.* **1992**, 4, 631.
- [11] S. Konishi, T. Nagasaki, K. Okuno, *J. Nucl. Mater.* **1995**, 223, 294.
- [12] J. C. Gachon, J. Hertz, *Calphad-Computer Coupling of Phase Diagrams and Thermochemistry*, Vol. 7, Pergamon Press, Cambridge, MA **1983**, pp. 1–12.
- [13] Z. Yao, X. Xiao, Z. Liang, X. Huang, H. Kou, W. Luo, C. Chen, L. Chen, *J. Mater. Chem. A* **2020**, 8, 9322.
- [14] M. Wu, J. Wang, P. Li, C. Hu, X. Tian, J. Song, *Materials* **2020**, 13, 3977.
- [15] Z. Liang, Z. Yao, X. Xiao, H. Kou, W. Luo, C. Chen, L. Chen, *J. Alloys Compd.* **2020**, 848, 156618.
- [16] Z. Yao, Z. Liang, X. Xiao, X. Huang, J. Liu, X. Wang, J. Zheng, H. Kou, W. Luo, C. Chen, L. Chen, *Mater. Today Energy* **2020**, 18, 100554.
- [17] Z. Liang, X. Xiao, Z. Yao, H. Kou, W. Luo, C. Chen, L. Chen, *Int. J. Hydrog. Energy* **2019**, 44, 28242.
- [18] Z. Liang, Z. Yao, X. Xiao, X. Wang, H. Kou, W. Luo, C. Chen, L. Chen, *Mater. Today Energy* **2021**, 20, 100645.
- [19] Z. Yao, Z. Liang, X. Xiao, J. Qi, J. He, X. Huang, H. Kou, W. Luo, C. Chen, L. Chen, *Renew. Energy* **2022**, 187, 500.
- [20] Z. Liang, Z. Yao, R. Li, X. Xiao, Z. Ye, X. Wang, J. Qi, J. Bi, X. Fan, H. Kou, W. Luo, C. Chen, L. Chen, *J. Energy Chem.* **2022**, 69, 397.
- [21] J. Qi, Z. Liang, X. Xiao, Z. Yao, P. Zhou, R. Li, L. Lv, X. Zhang, H. Kou, X. Huang, W. Luo, C. Chen, L. Chen, *Chem. Eng. J.* **2023**, 455, 140571.
- [22] M. Hara, T. Okabe, K. Mori, K. Watanabe, *Fusion Eng. Des.* **2000**, 49–50, 831.
- [23] L. Peng, C. Jiang, Q. Xu, X. Wu, *Fusion Eng. Des.* **2013**, 88, 299.
- [24] H. Kou, G. Sang, W. Luo, Z. Huang, D. Meng, G. Zhang, J. Deng, Z. Luo, W. He, C. Hu, *Int. J. Hydrog. Energy* **2015**, 40, 10923.
- [25] G. Yang, W. Liu, X. Han, H. Han, Y. Qian, Y. Zeng, X. Wu, J. Qiu, H. Yin, W. Liu, Y. Li, *Int. J. Hydrog. Energy* **2017**, 42, 15782.
- [26] G. Yang, W. Liu, J. Tan, S. Wu, J. Qiu, H. Cheng, H. Yin, N. Qian, Y. Huang, X. Wu, W. Liu, Y. Li, *Int. J. Hydrog. Energy* **2018**, 43, 10410.
- [27] J. Liu, T. Gao, Q. Wang, L. Wan, G. Sang, G. Zhang, H. Han, *Int. J. Hydrog. Energy* **2020**, 45, 28985.
- [28] Y. Yang, L. Wang, *Int. J. Hydrog. Energy* **2022**, 47, 24398.
- [29] S. Konishi, T. Nagasaki, T. Hayashi, K. Okuno, *J. Nucl. Mater.* **1995**, 223, 300.
- [30] T. B. Flanagan, H. Noh, S. Luo, *J. Alloys Compd.* **2016**, 677, 163.
- [31] C. E. Lundin, F. E. Lynch, C. B. Magee, *J. Less Common Met.* **1977**, 56, 19.
- [32] J. Prigent, J. M. Joubert, M. Gupta, *J. Solid State Chem.* **2011**, 184, 123.
- [33] F. A. Kuijpers, H. H. Vanmal, *J. Less Common Met.* **1971**, 23, 395.
- [34] H. E. Kissinger, *Anal. Chem.* **1957**, 29, 1702.
- [35] R. A. Jat, R. Singh, S. Pati, P. U. Sastry, A. Das, R. Agarwal, S. C. Parida, *Int. J. Hydrog. Energy* **2017**, 42, 8089.
- [36] Z. Yao, X. Xiao, Z. Liang, H. Kou, W. Luo, C. Chen, L. Jiang, L. Chen, *J. Alloys Compd.* **2019**, 784, 1062.
- [37] X. Gu, F. Wang, J. Cheng, X. Zeng, H. Kou, *Int. J. Hydrog. Energy* **2023**, 48, 26276.
- [38] N. Bekris, M. Sirc, *Fusion Sci. Technol.* **2012**, 62, 50.
- [39] R. A. Jat, R. Singh, S. C. Parida, A. Das, R. Agarwal, K. L. Ramakumar, *Int. J. Hydrog. Energy* **2014**, 39, 15665.
- [40] K. Zhang, F. Wang, X. Zeng, B. Zhang, H. Kou, *Int. J. Hydrog. Energy* **2020**, 45, 9877.
- [41] Y.-W. You, J. Yu, H. Yuan, Y. Xu, X. Wu, J. Sun, J. Wang, Q. F. Fang, C. S. Liu, *Int. J. Hydrog. Energy* **2020**, 45, 14028.
- [42] C. Song, F. Ding, R. Ye, J. Song, H. Zong, X. Chen, L. Zhou, *Int. J. Hydrog. Energy* **2023**, 48, 23607.
- [43] Q.-J. Li, H. Sheng, E. Ma, *Nat. Commun.* **2019**, 10, 806.
- [44] C. N. Saikrishna, K. V. Ramaiah, S. K. Bhaumik, *Mater. Sci. Eng. A* **2006**, 428, 217.
- [45] H. Kou, W. Luo, Z. Huang, G. Sang, C. Hu, C. Chen, G. Zhang, D. Luo, M. Liu, S. Zheng, *Int. J. Hydrog. Energy* **2016**, 41, 10811.
- [46] G. Kresse, J. Furthmüller, *Phys. Rev. B* **1996**, 54, 11169.
- [47] T. P. Hardcastle, C. R. Seabourne, R. Zan, R. M. D. Brydson, U. Bangert, Q. M. Ramasse, K. S. Novoselov, A. J. Scott, *Phys. Rev. B* **2013**, 87, 195430.
- [48] K. Momma, F. Izumi, *J. Appl. Crystallogr.* **2011**, 44, 1272.